Chapter 1

Data Analysis

The signature of GGM SUSY particle production in this search is an excess of two-photon events with high $\not{E}_T$ above the Standard Model background. $\not{E}_T$ is reconstructed using the particle flow algorithm as described in Sec. **??**. Candidate two-photon events, as well as control events, are selected according to the offline object criteria presented in Secs. **??** , **??**, and **??**; the event quality criteria in Sec. **??**; and the trigger requirements in Sec. **??**. These are summarized in Table 1.1.

Table 1.1: Selection criteria for $\gamma\gamma$, $e\gamma$, ee, and $f\!f$ events.

Variable	Cut			
	$\gamma\gamma$	$e\gamma$	ee	$f\!f$
HLT match	IsoVL	IsoVL	IsoVL	IsoVL || R9Id
E_T	$> 40/$ > 25 GeV	$> 40/$ > 25 GeV	$> 40/$ > 25 GeV	$> 40/$ > 25 GeV
SC $|\eta|$	< 1.4442	< 1.4442	< 1.4442	< 1.4442
H/E	< 0.05	< 0.05	< 0.05	< 0.05
$R9$	< 1	< 1	< 1	< 1
Pixel seed	No/No	Yes/No	Yes/Yes	No/No
I_{comb}, $\sigma_{i\eta i\eta}$	< 6 GeV && < 0.011	< 6 GeV && < 0.011	< 6 GeV && < 0.011	< 20 GeV && $(\geq 6$ GeV || $\geq 0.011)$
JSON	Yes	Yes	Yes	Yes
No. good PVs	≥ 1	≥ 1	≥ 1	≥ 1
ΔR_{EM}	> 0.6	> 0.6	> 0.6	> 0.6
$\Delta\phi_{\text{EM}}$	≥ 0.05	≥ 0.05	≥ 0.05	≥ 0.05

This search utilizes 4.7 fb^{-1} of CMS data collected during the period April-December 2011, corresponding to the following datasets [**?**]:

- `/Photon/Run2011A-05Jul2011ReReco-ECAL-v1/AOD`

- `/Photon/Run2011A-05Aug2011-v1/AOD`

- `/Photon/Run2011A-03Oct2011-v1/AOD`

- `/Photon/Run2011B-PromptReco-v1/AOD`

The search strategy is to model the backgrounds to the GGM SUSY signal using $\not{E}_T$ shape templates derived from the control samples, and then to look for a high-$\not{E}_T$ excess above the estimated background in the $\gamma\gamma$ sample. There are two categories of backgrounds: QCD processes with no real $\not{E}_T$ and electroweak processes with real $\not{E}_T$ from neutrinos. The relevant QCD background processes are multijet production with at least two jets faking photons, photon + jet production with at least one jet faking a photon, and diphoton production. The relevant electroweak background processes, which are small compared to the QCD background, involve $W \to e\nu$ decay with a recoiling jet that fakes a photon or a real radiated photon (the W may come from the decay of a top quark in $t\bar{t}$ events). In both cases, the electron is misidentified as a photon due to a small inefficiency in reconstructing the electron pixel seed. The main diagrams contributing to the QCD(electroweak) backgrounds are shown in Figure 1.1(1.2).

1.1 Control Samples

Data control samples are used to model all of the backgrounds. The primary control sample used to model the QCD background is the ff sample, which is similar to the candidate $\gamma\gamma$ sample but with combined isolation or $\sigma_{i\eta i\eta}$ cuts inverted. The cuts
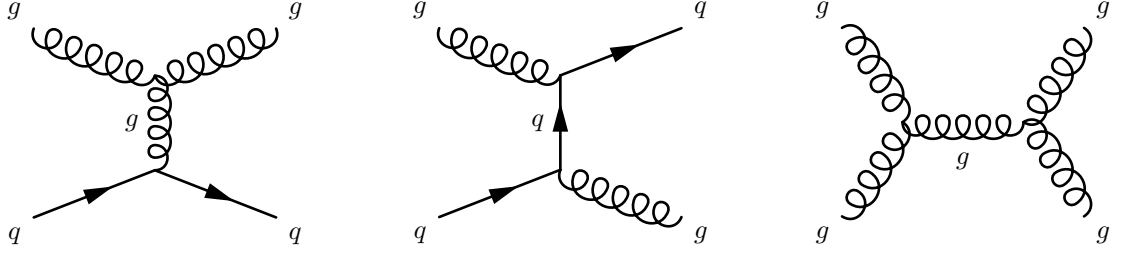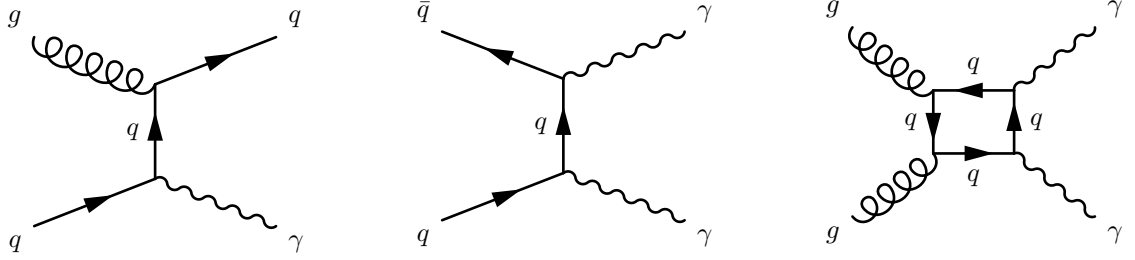
(a) Dijet production via gg and qg interactions.

(b) Photon + jet production via qg interactions.

(c) Diphoton production via $q\bar{q}$ and gg interactions.

Figure 1.1: Representative Feynman diagrams of some QCD backgrounds to the GGM SUSY search.

on these variables are used to distinguish between photons and jets, so by inverting those cuts, the resulting ff sample becomes enriched with QCD dijets. Because the fake photons are still required to pass a tight cut on H/E, they are guaranteed to be very electromagnetic jets, with an EM energy scale and resolution similar to that of the candidate photons. This insures that the resulting estimate of the $\not{E}_T$ shape does not have too long of a tail from severe HCAL mis-measurements that are actually rare in the $\gamma\gamma$ sample.

As a cross-check, the ee sample is also used to model the QCD background. This sample of Z decays should have no true $\not{E}_T$, just like the ff sample, and the electron definition (differing from the photon definition only in the presence of a pixel seed) insures that the electron energy scale and resolution is similar to that of the photon.

Finally, the $e\gamma$ sample is used to model the electroweak background from $W \to e\nu$ decays. The $e\gamma$ $\not{E}_T$ distribution is scaled by the electron→photon misidentification

(a) $W\gamma$ production.
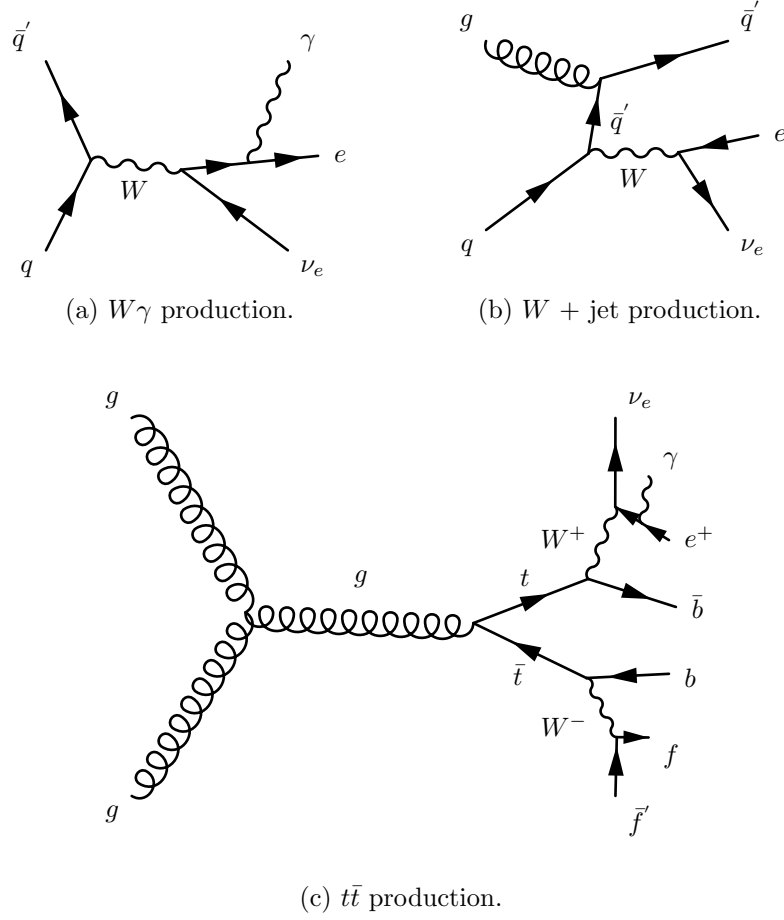
(b) W + jet production.

(c) $t\bar{t}$ production.

Figure 1.2: Representative Feynman diagrams of some electroweak backgrounds to the GGM SUSY search.

rate to predict the number of $W\gamma$, W + jet, and $t\bar{t}$ events in the $\gamma\gamma$ sample.

The remainder of this chapter describes the data analysis procedures and the final results of the search. Sec. 1.2 addresses the QCD background estimation. Sec. 1.3 addresses the electroweak background estimation. The chapter concludes with a discussion of systematic errors in Sec. 1.4 and a presentation of the final results in Sec. 1.5.

1.2 Modeling the QCD Background

1.2.1 Outline of the Procedure

Due to the fact that the CMS ECAL energy resolution is much better than the HCAL energy resolution, the energies of the two candidate photons in the events of the $\gamma\gamma$ sample are typically measured to far greater accuracy and precision than the energy of the hadronic recoil in those events. Therefore, fake $\not{E}_T$ in the $\gamma\gamma$ sample is almost entirely the result of hadronic mis-measurement in QCD dijet, photon + jet, and diphoton events. The strategy employed to model this background is to find a control sample in data consisting of two well-measured EM objects, just like the candidate $\gamma\gamma$ sample, and assign each event a weight to account for the underlying kinematic differences between the control and candidate samples. Once the reweighted $\not{E}_T$ spectrum of the control sample is created, it is then normalized in the low-$\not{E}_T$ region, the assumption being that GGM SUSY does not predict a significant amount of events at low $\not{E}_T$. There are three aspects of this QCD background estimation procedure that bear highlighting:

Choice of control sample Since the underlying cause of $\not{E}_T$ in the candidate sample is mis-measured hadronic activity, a control sample with similar hadronic activity to the candidate sample should be chosen. Hadronic activity refers to number of jets, jet E_T, pileup, etc.

Reweighting The control sample is reweighted so that its $\not{E}_T$ spectrum appears as it would if the control sample had the same kinematic properties as the candidate $\gamma\gamma$ sample (i.e. particle p_T and η distributions, etc.). By choosing an appropriate control sample and reweighting it, the control $\not{E}_T$ distribution should now match both the hadronic activity and the kinematics of the candidate sample.

Normalization Finally, the control $\not{E}_T$ distribution is normalized in a region of low $\not{E}_T$, where contamination from the expected GGM SUSY signal is small. This implies an extrapolation of the low-$\not{E}_T$ QCD background prediction to the high-$\not{E}_T$ signal region.

As explained in the beginning of this chapter, the ff sample is used as the primary QCD control sample, while the ee sample is used as a cross-check. Both samples have two well-measured EM objects per event, no real $\not{E}_T$, and similar hadronic activity to the $\gamma\gamma$ sample. Figures 1.3- 1.8 show a comparison of the shapes of some distributions relevant to hadronic activity between the $\gamma\gamma$, ee, and ff samples. In general, the ee sample has less hadronic activity than the $\gamma\gamma$ and ff samples, as shown by the more steeply falling ee distributions in Figs. 1.3, 1.4, 1.5, and 1.6. In addition to the kinematic reweighting, there is also a reweighting by number of jets per event, which attempts to correct for this difference (see Sec. 1.2.2).

1.2.2   Reweighting

To reweight the control sample events to match the kinematics of the candidate sample events, a weight based on the p_T of the di-EM-object system and the number of jets in the event is used. As explained in Sec. 1.2.1, $\not{E}_T$ in the $\gamma\gamma$, ff, and ee samples is due to the poorly measured hadronic recoil off the well-measured di-EM system. Therefore, the p_T of the di-EM system is a good handle on the true magnitude of the hadronic recoil, which affects the measured $\not{E}_T$. The di-EM system is depicted
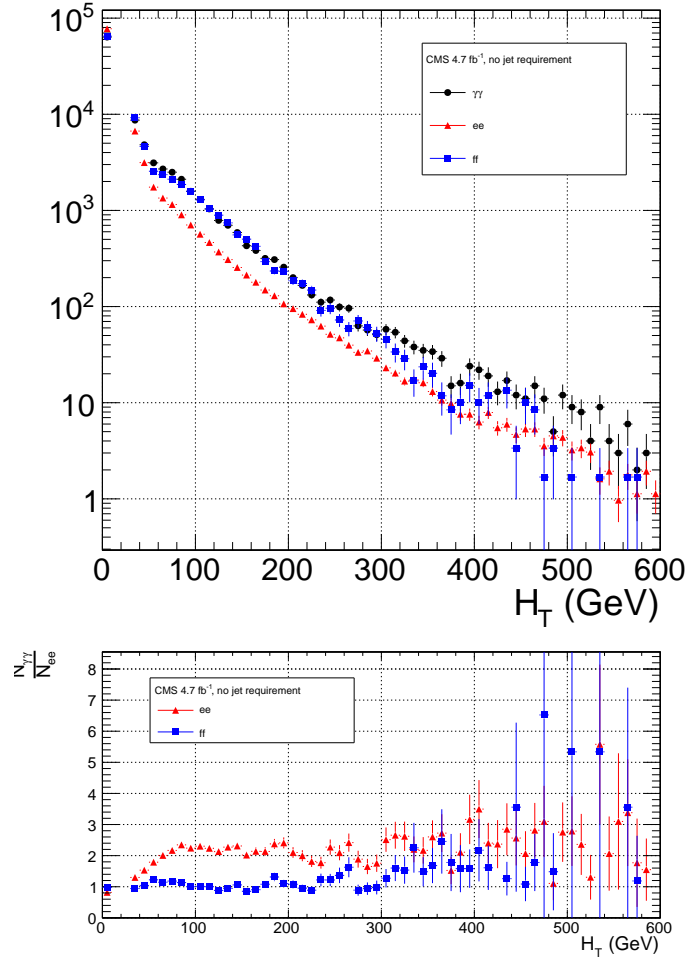
Figure 1.3: H_T, defined as the scalar sum of corrected jet E_T for jets defined as in Table 1.2. $\gamma\gamma$ is in black, ee (81 GeV $\leq m_{ee} <$ 101 GeV) is in red, and ff is in blue. The ee and ff distributions are normalized to the number of events in the $\gamma\gamma$ distribution. Errors are statistical only.
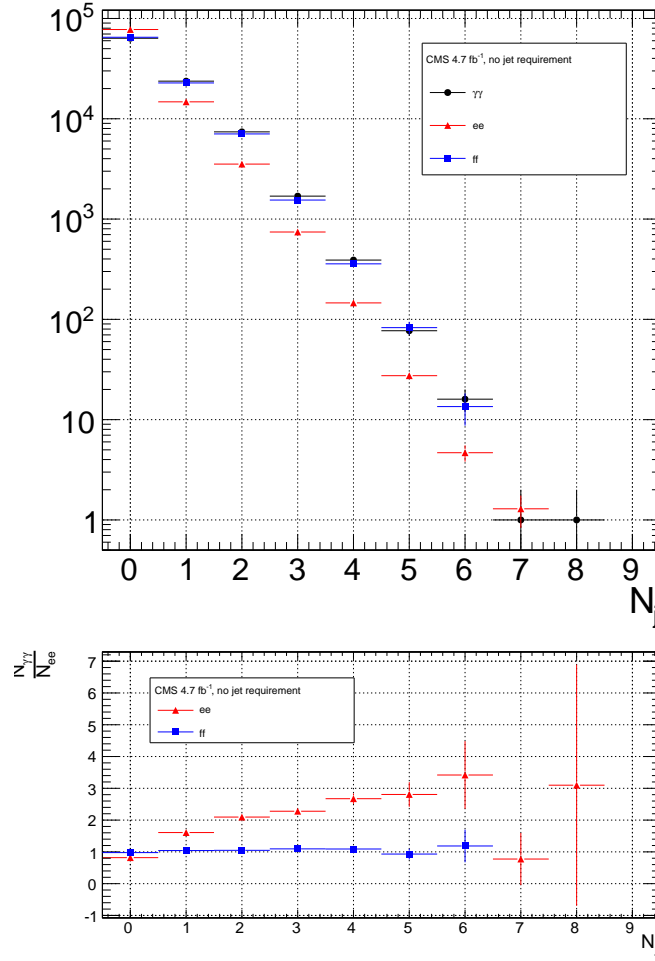
Figure 1.4: Number of jets per event for jets defined as in Table 1.2. $\gamma\gamma$ is in black, *ee* (81 GeV $\leq m_{\text{ee}} <$ 101 GeV) is in red, and *ff* is in blue. The *ee* and *ff* distributions are normalized to the number of events in the $\gamma\gamma$ distribution. Errors are statistical only.
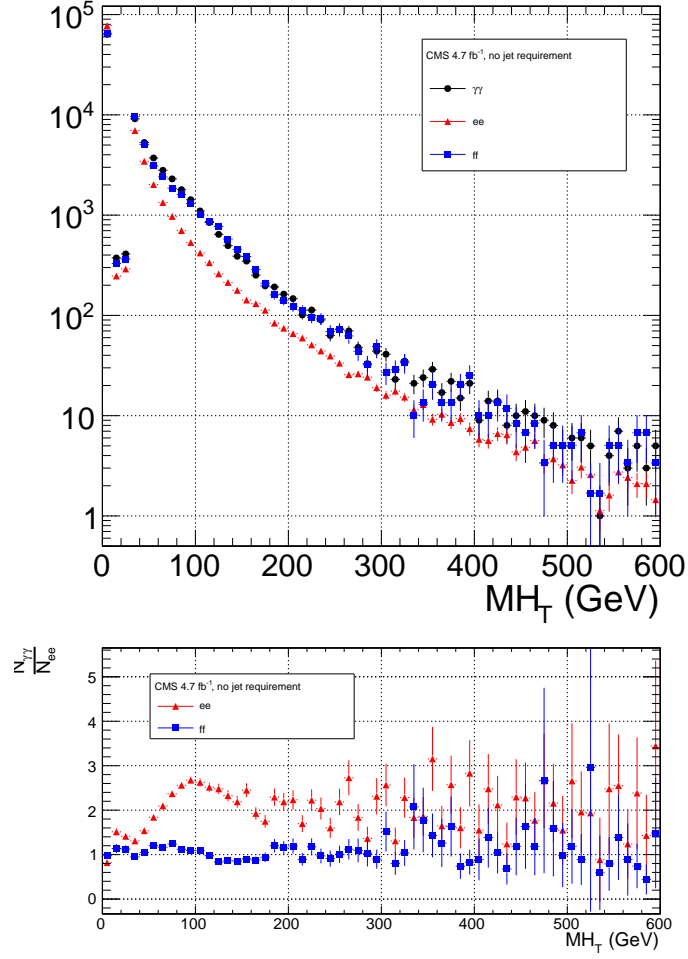
Figure 1.5: $\not{H}_T$, defined as the magnitude of the negative vectorial sum of corrected jet E_T for jets defined as in Table 1.2. $\gamma\gamma$ is in black, *ee* (81 GeV $\leq m_{ee} <$ 101 GeV) is in red, and *ff* is in blue. The *ee* and *ff* distributions are normalized to the number of events in the $\gamma\gamma$ distribution. Errors are statistical only.
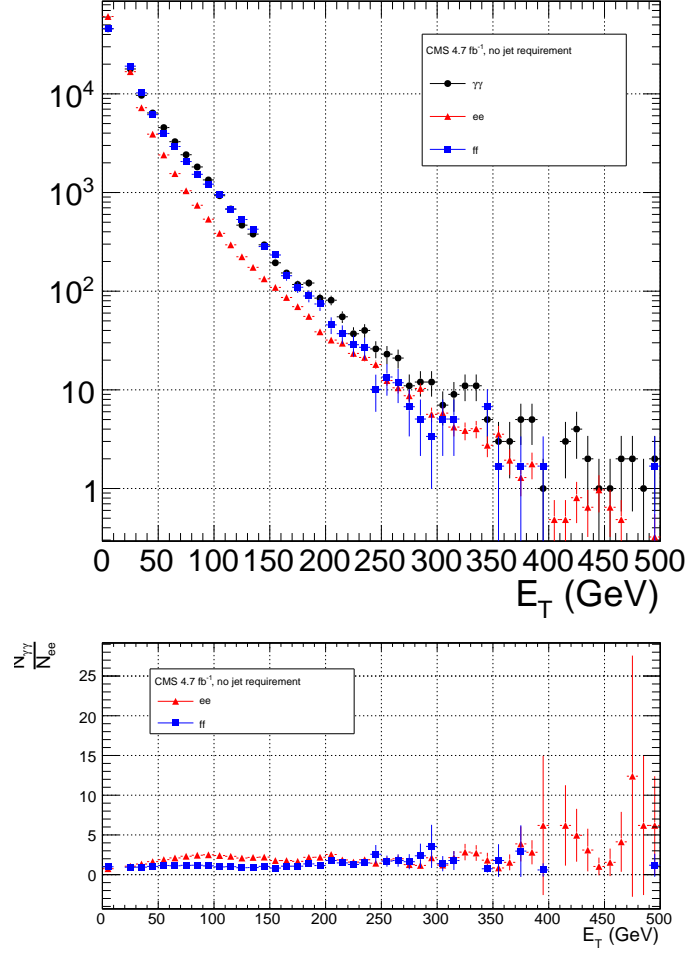
Figure 1.6: Corrected E_T for the jet with the largest corrected E_T per event, for jets defined as in Table 1.2 (excluding the p_T requirement). $\gamma\gamma$ is in black, ee (81 GeV $\leq m_{ee} < 101$ GeV) is in red, and ff is in blue. The ee and ff distributions are normalized to the number of events in the $\gamma\gamma$ distribution. Errors are statistical only.

Figure 1.7: ρ (average pileup energy density in the calorimeters per unit $\eta \cdot \phi$, cf. Sec. **??**). $\gamma\gamma$ is in black, *ee* (81 GeV $\leq m_{ee} < 101$ GeV) is in red, and *ff* is in blue. The *ee* and *ff* distributions are normalized to the number of events in the $\gamma\gamma$ distribution. Errors are statistical only.
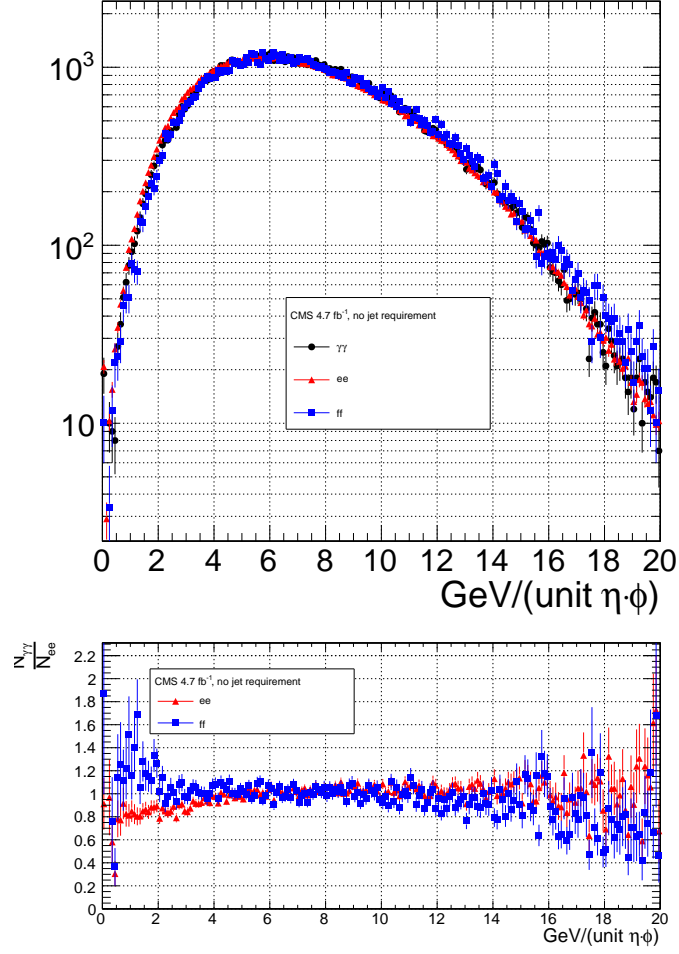
Figure 1.8: Number of good reconstructed primary vertices per event according to the criteria of Sec. **??**. $\gamma\gamma$ is in black, *ee* (81 GeV $\leq m_{\mathrm{ee}} < 101$ GeV) is in red, and *ff* is in blue. The *ee* and *ff* distributions are normalized to the number of events in the $\gamma\gamma$ distribution. Errors are statistical only.
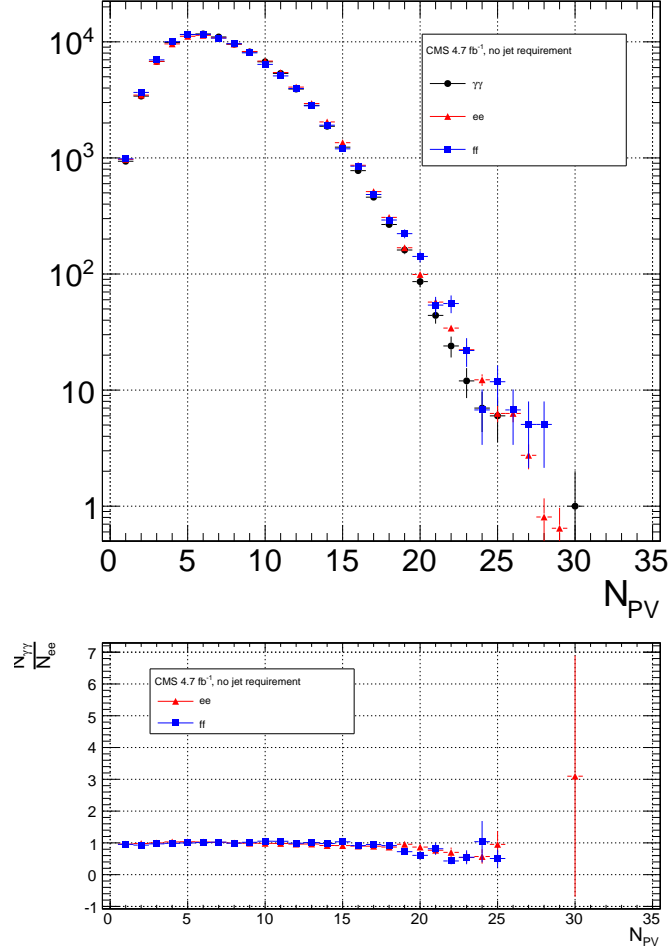
Table 1.2: Definition of HB/HE/HF hadronic jets.

Variable	Cut
Algorithm	`L1FastL2L3Residual` corrected PF (cf. Sec. **??**)
p_T	> 30 GeV
$|\eta|$	< 5.0
Neutral hadronic energy fraction	< 0.99
Neutral electromagnetic energy fraction	< 0.99
Number of constituents	> 1
Charged hadronic energy	> 0.0 GeV if $|\eta| < 2.4$
Number of charged hadrons	> 0 if $|\eta| < 2.4$
Charged electromagnetic energy fraction	< 0.99 if $|\eta| < 2.4$
ΔR to nearest PF electron[a], muon[b], or one of the two primary EM objects	> 0.5

[a]A PF electron is defined as an electron reconstructed with the PF algorithm [**?**] with $p_T > 15$ GeV, $|\eta| < 2.6$, and $(I_{\text{charged}} + I_{\text{photon}} + I_{\text{neutral}})/p_T < 0.2$, where $I_{\text{charged}}(I_{\text{photon}})(I_{\text{neutral}})$ is the sum of PF charged hadron(PF photon)(PF neutral hadron) momenta in a $\Delta R = 0.4$ cone around the PF electron.

[b]Muons are reconstructed [**?**] from a combination of muon station and inner tracker hits. Here, a muon must have track $\chi^2 < 10$, at least one good muon station hit, inner track transverse impact parameter < 0.02 cm, inner track longitudinal impact parameter < 0.5 cm, $p_T > 15$ GeV, $|\eta| < 2.6$, and $(I_{\text{ECAL}} + I_{\text{HCAL}} + I_{\text{track}})/p_T < 0.2$, where $I_{\text{ECAL}}(I_{\text{HCAL}})(I_{\text{track}})$ is the sum of ECAL(HCAL)(track) momenta in a $\Delta R = 0.3$ cone around the muon.

EM objects (well measured
kinematics, no fake ME$_T$)

di-EM p$_T$ (well-measured handle on the
kinematics of the jet system)

Most energetic EM object

2nd most energetic EM object

z (beam
direction)

y

x

Jets (poorly measured
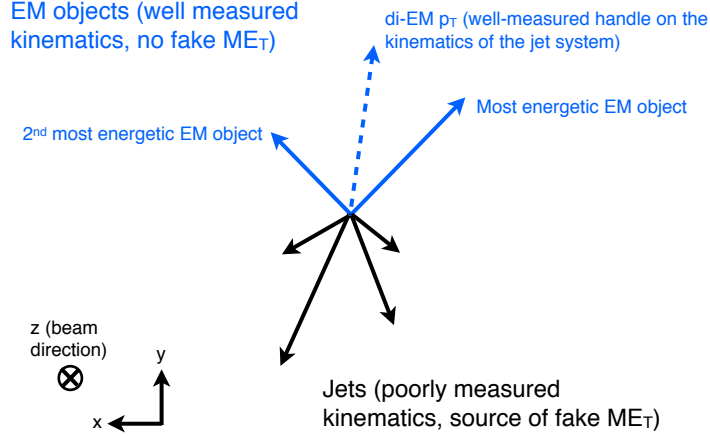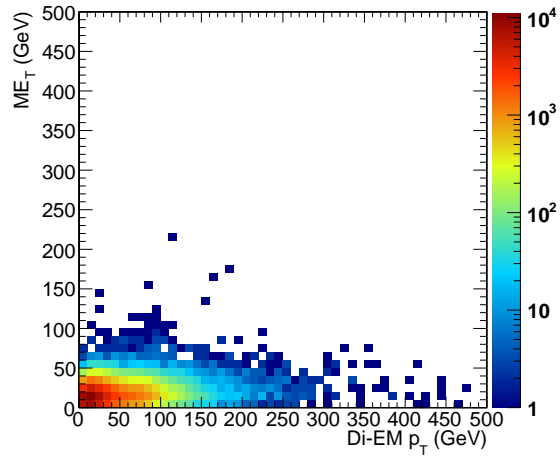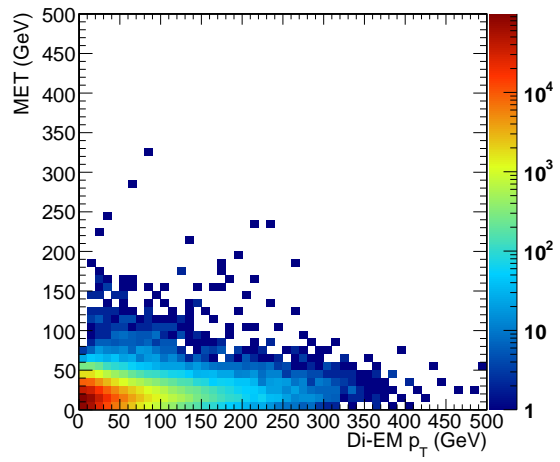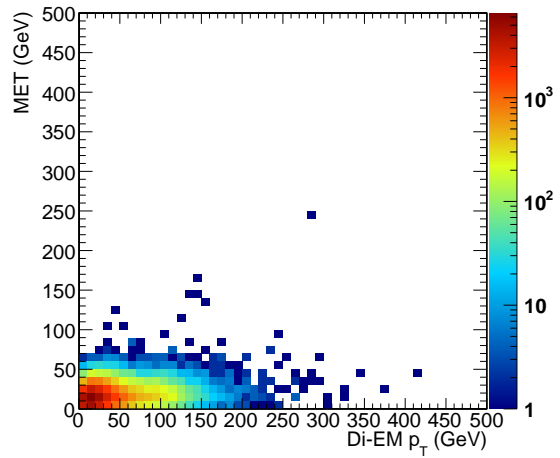kinematics, source of fake ME$_T$)

Figure 1.9: Cartoon showing the di-EM system in blue and the hadronic recoil in black. The di-EM p_T (dashed blue line) is used to reweight the control sample kinematic properties to match those of the candidate $\gamma\gamma$ sample.

.

in Figure 1.9. As shown in Figure 1.10, $\not{E}_T$ is largely uncorrelated with di-EM p_T, so there is little danger of reweighting away a true signal excess.

Whereas the di-EM p_T reweighting accounts for differences in production kinematics between the control and $\gamma\gamma$ samples, a simultaneous reweighting based on the number of jets in the event accounts for differences in hadronic activity between the samples, especially between ee and $\gamma\gamma$ (cf. Figs. 1.3- 1.8). Jets are defined as in Table **??**. Figure 1.11 shows the effect of reweighting by number of jets per event, which is to increase(decrease) the tail of the $ee(\textit{ff})$ $\not{E}_T$ spectrum.

Although the electron and photon energies are well measured by the ECAL, the ECAL-only measurement of the fake photon energy (cf. Sec **??**) is biased slightly low due to the fact that fakes (which are really jets) tend to deposit some energy in the HCAL. This can be seen in Figs. 1.12 and 1.13, which show the relative difference between the ECAL-only E_T measurement and the PF E_T measurement vs. EMF for electrons, photons, and fakes. PF E_T is defined as the `L1Fast`-corrected E_T of the nearest PF jet with $p_T \geq 20$ GeV (i.e., the E_T of the PF jet object reconstructed from the same ECAL shower as the fake photon). On average, the high-EMF fakes, which

(a) $\gamma\gamma$.

(b) ee.

(c) ff.

Figure 1.10: $\not{E}_T$ vs. di-EM p_T.
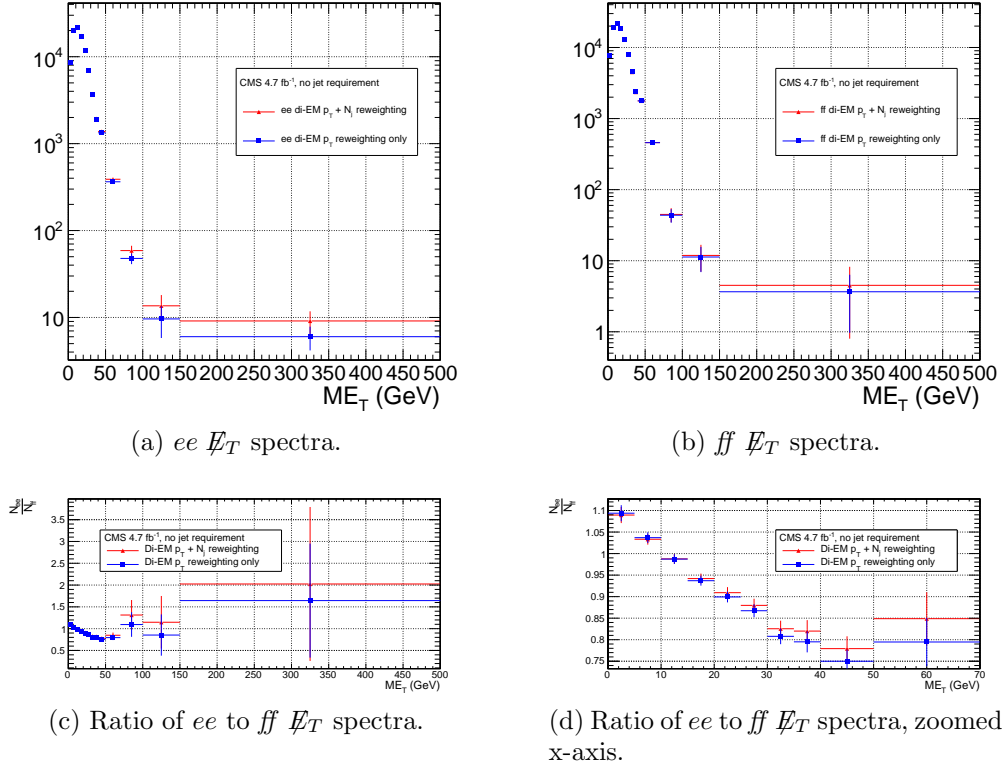
(a) *ee* $\not{E}_T$ spectra.

(b) *ff* $\not{E}_T$ spectra.

(c) Ratio of *ee* to *ff* $\not{E}_T$ spectra.

(d) Ratio of *ee* to *ff* $\not{E}_T$ spectra, zoomed x-axis.

Figure 1.11: $\not{E}_T$ spectra of the reweighted *ee* ($81\,\mathrm{GeV} \leq m_{\mathrm{ee}} < 101\,\mathrm{GeV}$) and *ff* control samples. Blue squares indicate di-EM p_T reweighting only; red triangles indicate di-EM p_T + number of jets reweighting. PF p_T (cf. p. 15) is used to calculate the di-EM p_T. The full normalization procedure is employed, along with *ee* sideband subtraction (discussed at the end of this section). Error bars are statistical only.

make up the bulk of the sample, tend to deposit a few percent more energy in the HCAL than the electrons or photons. This energy is recovered by the PF algorithm. For this reason, the PF p_T is used in the calculation of di-EM p_T rather than the ECAL-only p_T.[1] This leads to a modest improvement in the agreement between the ee and ff $\not{E}_T$ spectra, as shown in Figure 1.14.

The control sample event weights are defined as

$$w_{ij} = \frac{N_{\text{control}}}{N_{\gamma\gamma}} \frac{N_{\gamma\gamma}^{ij}}{N_{\text{control}}^{ij}} \tag{1.1}$$

where i runs over the number of di-EM p_T bins, j runs over the number of jet bins, N_{control} is the total number of events in the control sample, $N_{\gamma\gamma}$ is the total number of events in the $\gamma\gamma$ sample, $N_{\gamma\gamma}^{ij}$ is the number of $\gamma\gamma$ events in the ith di-EM p_T bin and j^{th} jet bin, and N_{control}^{ij} is the number of control sample events in the ith di-EM p_T bin and j^{th} jet bin. The effect of the reweighting is more significant for the ee sample than for the ff sample, as shown in Figure 1.15.

The ee sample contains a non-negligible background of $t\bar{t}$ events in which both W bosons decay to electrons. These events have significant real $\not{E}_T$ from the two neutrinos (unlike the $\gamma\gamma$ events), and therefore inflate the background estimate at high $\not{E}_T$. In order to remove the $t\bar{t}$ contribution from the ee sample, a sideband subtraction method is employed.

Only events in the ee sample with $81 \text{ GeV} \leq m_{\text{ee}} < 101 \text{ GeV}$, where m_{ee} is the di-electron invariant mass, are used in the QCD background estimate. This choice maximizes the ratio of Z signal to background. The sidebands used to estimate the background contribution within the Z window are defined such that $71 \text{ GeV} \leq m_{\text{ee}} < 81 \text{ GeV}$ and $101 \text{ GeV} \leq m_{\text{ee}} < 111 \text{ GeV}$.

---

[1]In the few events ($\mathcal{O}(10^{-3})$) in which two PF jet objects, corresponding to the two electrons or fakes, are not found, the ECAL-only p_T is used.
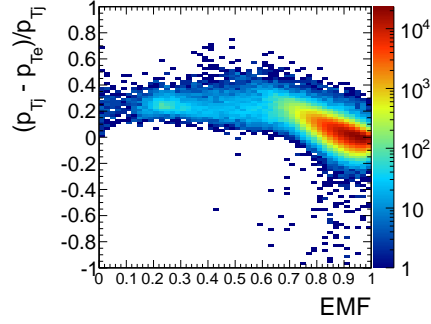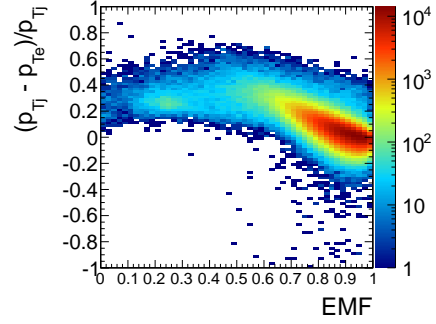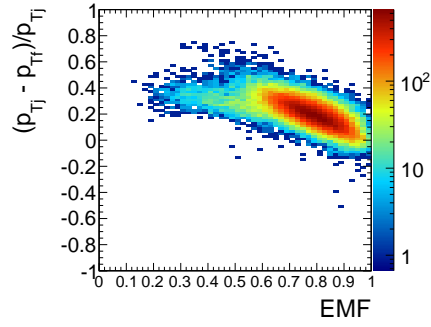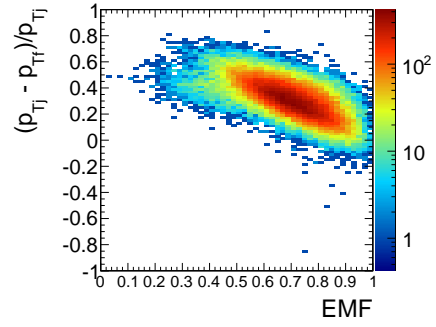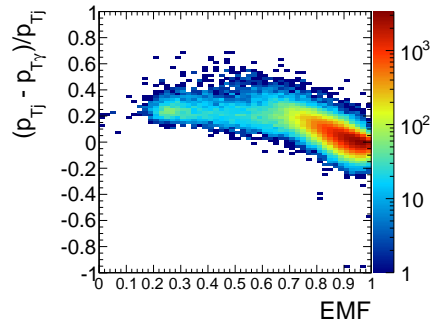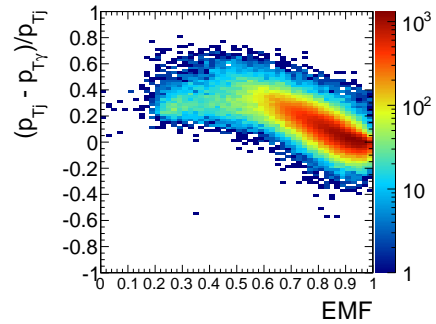
(a) Leading electron in *ee* events.

(b) Trailing electron in *ee* events.

(c) Leading fake in *ff* events.

(d) Trailing fake in *ff* events.

(e) Leading photon in $\gamma\gamma$ events.

(f) Trailing photon in $\gamma\gamma$ events.

Figure 1.12: Relative difference between the ECAL-only E_T measurement and the PF E_T measurement vs. EMF. PF E_T is defined in the text.
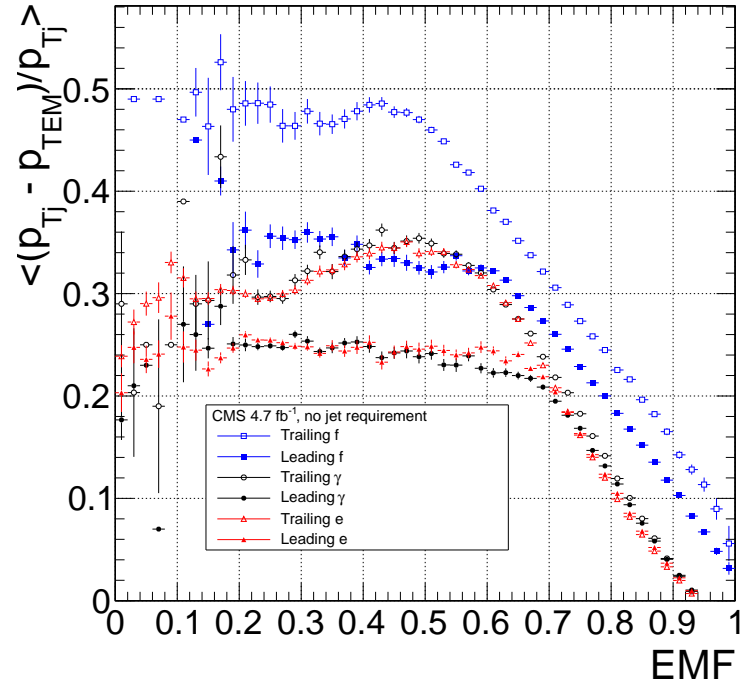
Figure 1.13: Average relative difference between the ECAL-only E_T measurement and the PF E_T measurement vs. EMF for the leading (filled marker) and trailing (open marker) electrons in *ee* events (red triangles), fakes in *ff* events (blue squares), and photons in $\gamma\gamma$ events (black circles). These are nothing more than profile histograms of Fig. 1.12. PF E_T is defined in the text. Error bars are statistical only.

(a) *ee* $\not{E}_T$ spectra.

(b) *ff* $\not{E}_T$ spectra.

(c) Ratio of *ee* to *ff* $\not{E}_T$ spectra.

(d) Ratio of *ee* to *ff* $\not{E}_T$ spectra, zoomed x-axis.

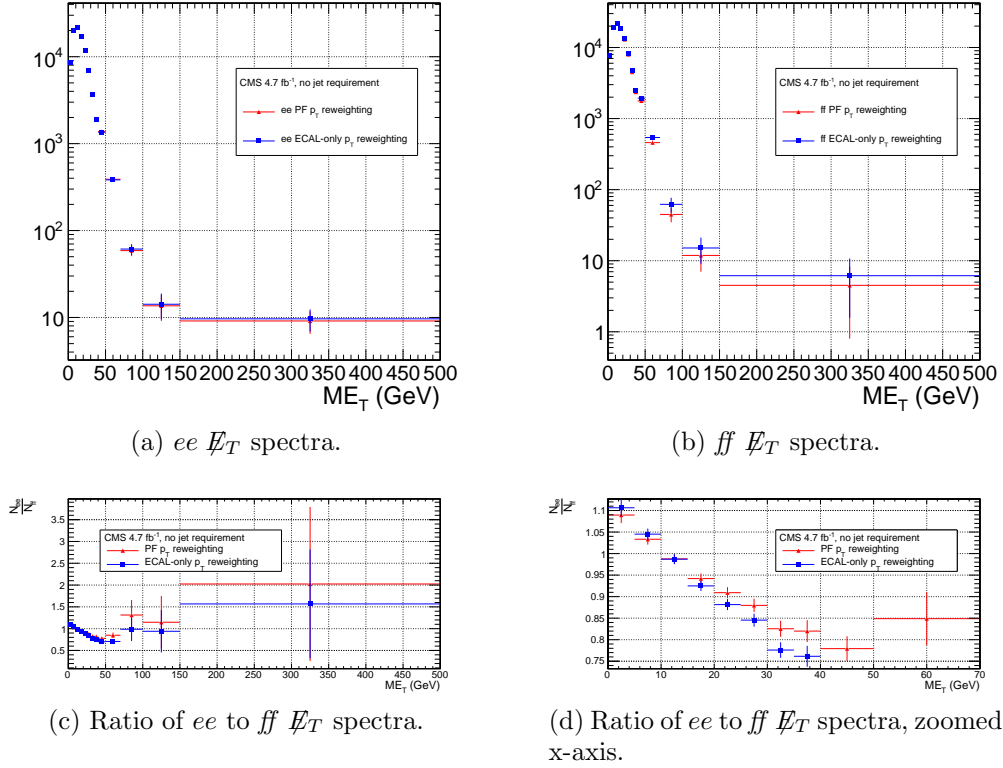Figure 1.14: $\not{E}_T$ spectra of the reweighted *ee* (81 GeV $\leq m_{ee} <$ 101 GeV) and *ff* control samples. Blue squares indicate reweighting using the ECAL-only p_T estimate; red triangles indicate reweighting using the PF p_T estimate. The full reweighting and normalization procedure is employed, along with *ee* sideband subtraction (discussed at the end of this section). Error bars are statistical only.

(a) *ee* $\not{E}_T$ spectra.

(b) *ff* $\not{E}_T$ spectra.

(c) Ratio of *ee* to *ff* $\not{E}_T$ spectra.

(d) Ratio of *ee* to *ff* $\not{E}_T$ spectra, zoomed x-axis.

Figure 1.15: $\not{E}_T$ spectra of the *ee* (81 GeV $\leq m_{ee} <$ 101 GeV) and *ff* control samples. Red triangles indicate full di-EM p_T + number of jets reweighting; blue squares indicate no reweighting. PF p_T (cf. p. 18) is used to calculate the di-EM p_T. The full normalization procedure is employed, along with *ee* sideband subtraction (discussed at the end of this section). Error bars are statistical only.
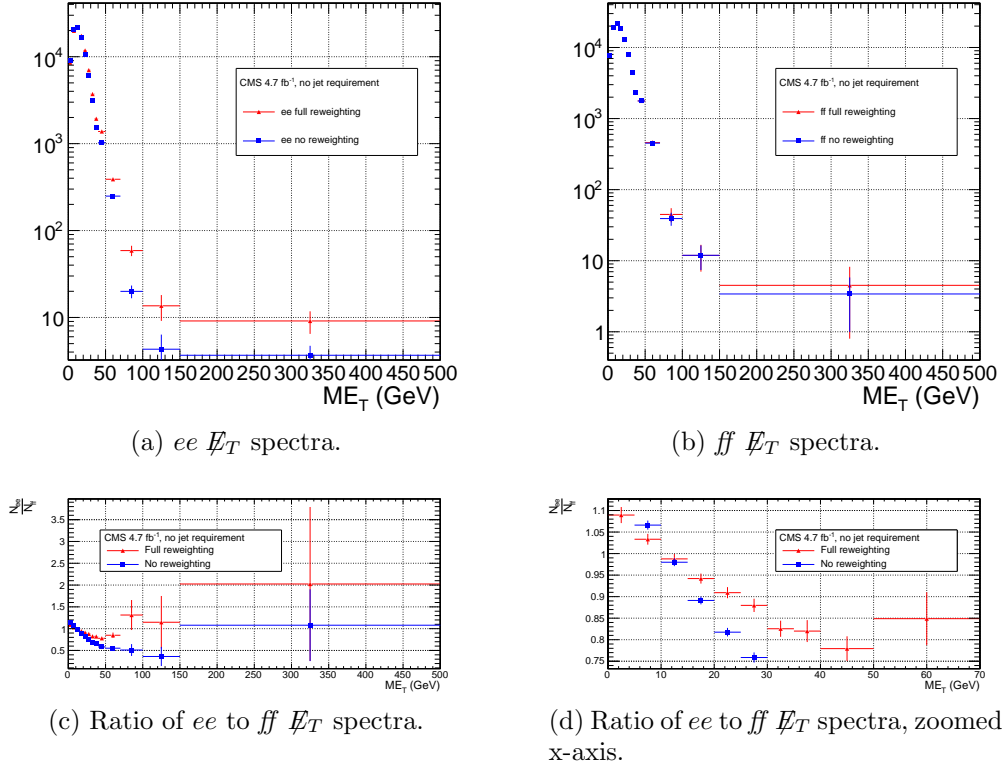
The full reweighting procedure is applied to the Z signal region and the two sideband regions independently. Only Z signal events are used in the calculation of the di-EM p_T weights for the Z signal region, and likewise only the events within a given sideband region are used in the calculation of the weights for that region. Assuming a constant $t\bar{t}$ background shape, the resulting reweighted sideband $\not{E}_T$ distributions are added together and subtracted from the reweighted Z signal $\not{E}_T$ distribution. The sideband subtracted Z signal $\not{E}_T$ distribution is then normalized as discussed in Secs. 1.2.1 and 1.2.3. The statistical and reweighting error from the sideband regions is propagated to the error on the final ee QCD $\not{E}_T$ estimate.

The di-EM p_T weights for the two ee sideband regions are shown in Figure 1.16. The overall scale of the weights, as well as the trend with di-EM p_T, is similar for the two regions (except at high di-EM p_T, where the statistics are poor anyway). Figure 1.17 shows the $\not{E}_T$ spectra for the two sideband regions and the Z signal region after subtraction. The shapes of the spectra indicate that the high-$\not{E}_T$ $t\bar{t}$ tail, present in the sideband distributions, was successfully subtracted from the Z signal distribution.

The ee (81 GeV $\leq m_{\text{ee}} < 101$ GeV), ff, and $\gamma\gamma$ di-EM p_T spectra for events with 0, 1, or ≥ 2 jets (as in Table **??**) are shown in Figure 1.18. Broad humps in the ff and $\gamma\gamma$ spectra are due to kinematic ΔR and p_T turn-ons that are suppressed in the ee sample due to the invariant mass cut. Figure 1.19 shows the weights applied to the ee (81 GeV $\leq m_{\text{ee}} < 101$ GeV) and ff $\not{E}_T$ spectra as a function of di-EM p_T and number of jets per event.

1.2.3 Normalization

After reweighting, the $\not{E}_T$ distributions of the QCD control samples are normalized to the $\not{E}_T < 20$ GeV region of the candidate $\gamma\gamma$ $\not{E}_T$ spectrum, where signal contamination is low. The normalization factor is $(N_{\gamma\gamma}^{\not{E}_T<20\text{GeV}} - N_{e\gamma}^{\not{E}_T<20\text{GeV}})/N_{\text{control}}^{\not{E}_T<20\text{GeV}}$,

(a) 71 GeV $\leq m_{\mathrm{ee}} < 81$ GeV, 0 jets.

(b) 71 GeV $\leq m_{\mathrm{ee}} < 81$ GeV, 1 jet.

(c) 71 GeV $\leq m_{\mathrm{ee}} < 81$ GeV, ≥ 2 jets.

(d) 101 GeV $\leq m_{\mathrm{ee}} < 111$ GeV, 0 jets.

(e) 101 GeV $\leq m_{\mathrm{ee}} < 111$ GeV, 1 jet.

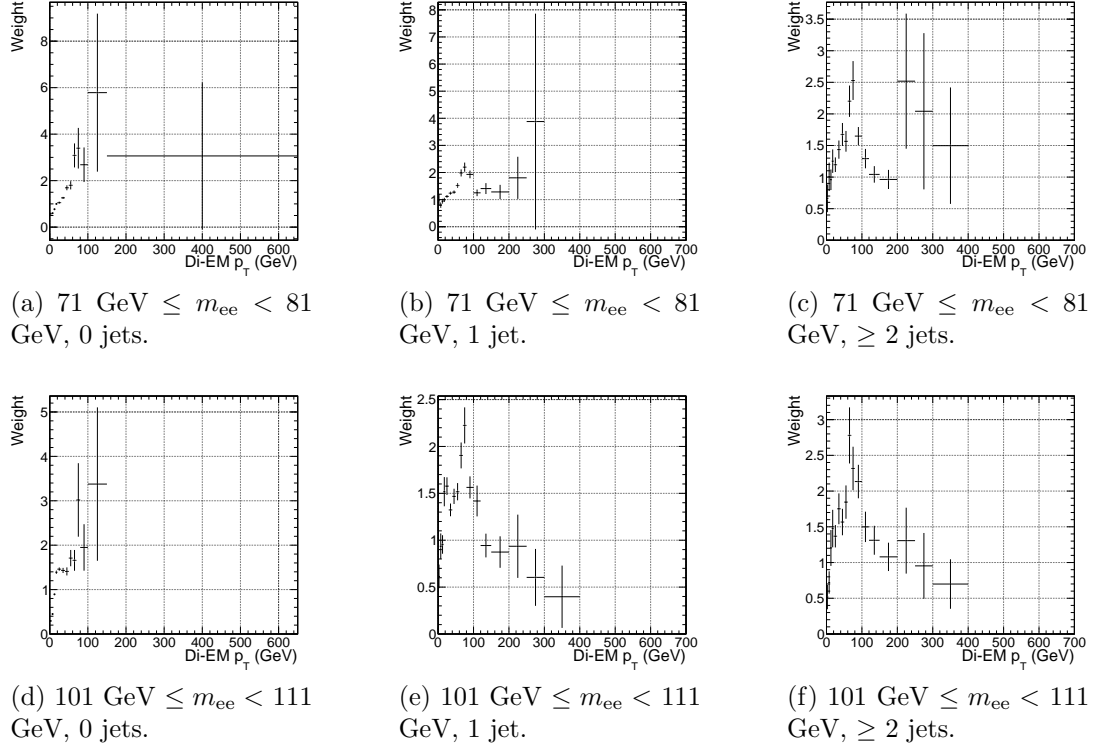(f) 101 GeV $\leq m_{\mathrm{ee}} < 111$ GeV, ≥ 2 jets.

Figure 1.16: *ee* sideband di-EM p_T weights for events with 0, 1, or ≥ 2 jets (as in Table **??**). Errors are statistical only.
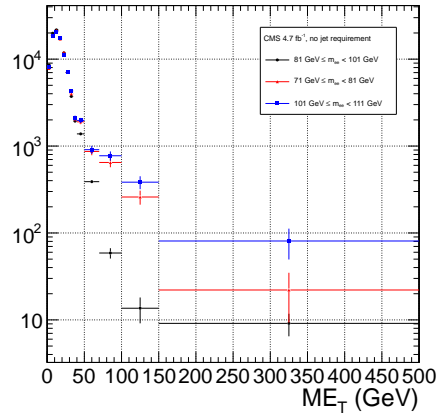
Figure 1.17: $\not{E}_T$ spectra of the *ee* sample for 71 GeV $\leq m_{\mathrm{ee}} < 81$ GeV (red triangles), 81 GeV $\leq m_{\mathrm{ee}} < 101$ GeV (black circles), and 101 GeV $\leq m_{\mathrm{ee}} < 111$ GeV (blue squares). The two sideband distributions (red and blue) and the Z signal distribution (black) are normalized to the total number of $\gamma\gamma$ events. Errors are statistical only.
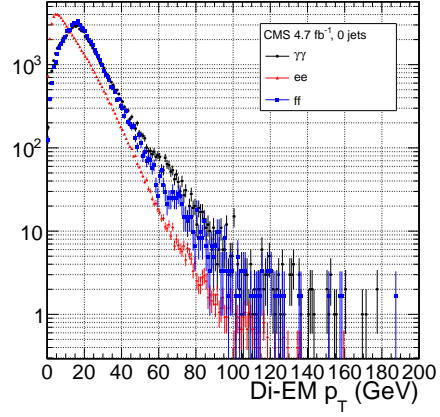
(a) 0 jets.
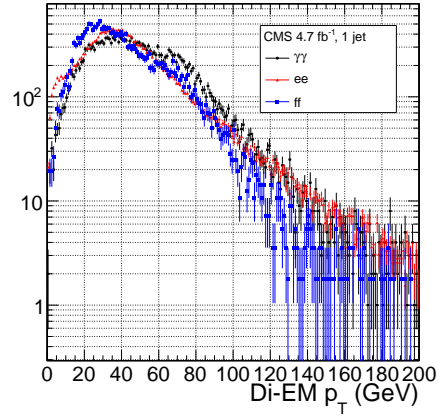
(b) 1 jet.

(c) ≥ 2 jets.

Figure 1.18: *ee* (81 GeV $\leq m_{\text{ee}} < 101$ GeV) (red triangles), *ff* (blue squares), and $\gamma\gamma$ (black circles) di-EM p_T spectra for events with 0, 1, or ≥ 2 jets (as in Table **??**). Errors are statistical only.

(a) *ee*, 0 jets.   (b) *ee*, 1 jet.   (c) *ee*, ≥ 2 jets.

(d) *ff*, 0 jets.   (e) *ff*, 1 jet.   (f) *ff*, ≥ 2 jets.

Figure 1.19: *ee* (81 GeV $\leq m_{\mathrm{ee}} < 101$ GeV) and *ff* di-EM p_T weights for events with 0, 1, or ≥ 2 jets (as in Table **??**). Errors are statistical only.

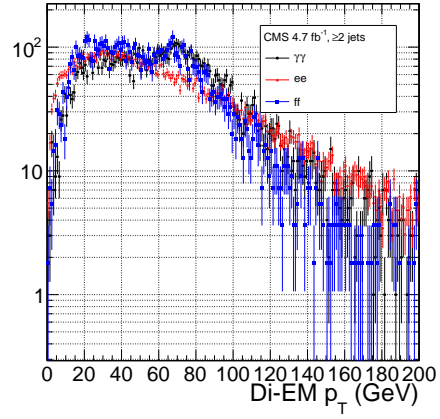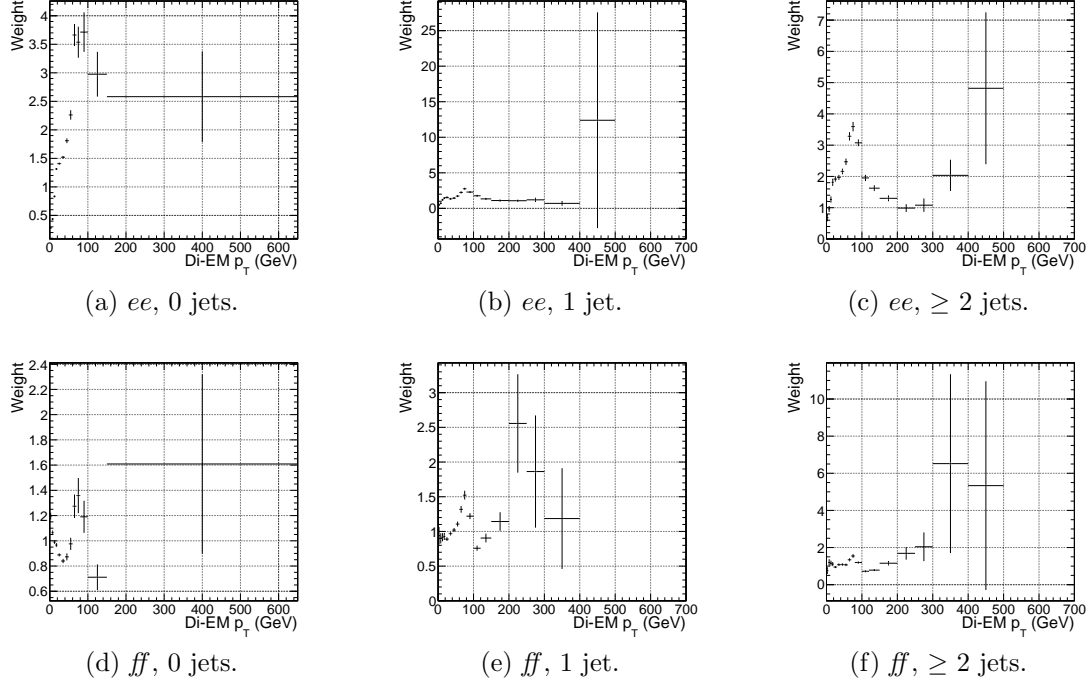where $N_{e\gamma}^{\not{E}_T < 20\mathrm{GeV}}$ is the expected number of electroweak background events with $\not{E}_T$ < 20 GeV (discussed in Section 1.3). The error on the QCD background prediction introduced by normalization is discussed in Sec. 1.4.

1.3   Modeling the Electroweak Background

$W\gamma$, W + jet, and $t\bar{t}$ processes in which the W decay electron is misidentified as a photon (due to a failure to properly associate a pixel seed to the electron candidate) can contribute significantly to the high-$\not{E}_T$ tail of the $\gamma\gamma$ $\not{E}_T$ spectrum. To estimate this background, the $e\gamma$ sample, which is enriched in $W \to e\nu$ decays, is scaled by $f_{e\to\gamma}/(1-f_{e\to\gamma})$, where $f_{e\to\gamma}$ is the rate at which electrons are misidentified as photons. The derivation of this scaling factor comes from the two equations

$$N_{e\gamma}^{W} = f_{e\to e}N_W \tag{1.2}$$

$$N_{\gamma\gamma}^{W} = (1 - f_{e\to e})N_W \tag{1.3}$$

where $N_{e\gamma}^{W}$ is the number of W events in the $e\gamma$ sample in which the electron was correctly identified, $f_{e\to e}$ is the probability to correctly identify an electron, N_W is the true number of triggered $W \to e\nu$ events, and $N_{\gamma\gamma}^{W}$ is the number of W events in the $\gamma\gamma$ sample in which the electron was misidentified as a photon. The contribution from $Z \to ee$ can be neglected (i.e. $f_{e\to\gamma}$ is small and the Z contribution involves $f_{e\to\gamma}^{2}$, since both electrons have to be misidentified). Since $f_{e\to e} = 1 - f_{e\to\gamma}$, solving for $N_{\gamma\gamma}^{W}$ gives

$$N_{\gamma\gamma}^{W} = \frac{f_{e\to\gamma}}{1 - f_{e\to\gamma}}N_{e\gamma}^{W} \tag{1.4}$$

$f_{e\to\gamma}$ is measured by fitting the Z peaks in the ee and $e\gamma$ samples. The number of Z events fitted in the ee and $e\gamma$ samples, respectively, is given by

$$N_{ee}^{Z} = (1 - f_{e\to\gamma})^{2}N_Z \tag{1.5}$$

$$N_{e\gamma}^{Z} = 2f_{e\to\gamma}(1 - f_{e\to\gamma})N_Z \tag{1.6}$$

where N_Z is the true number of triggered $Z \to ee$ events. Solving for $f_{e\to\gamma}$ gives

$$f_{e\to\gamma} = \frac{N_{e\gamma}^{Z}}{2N_{ee}^{Z} + N_{e\gamma}^{Z}} \tag{1.7}$$

A Crystal Ball function is used to model the Z signal shape in both the ee and $e\gamma$ samples, while an exponential convoluted with an error function (`RooCMSShape`, see Sec. **??**) is used to model the background shape. The fixed fit parameters are identical for the two samples, but the other parameters are allowed to float independently. Table 1.3 shows the values and ranges of the fixed and floating fit parameters, respectively.

Table 1.3: Parameter values for the signal and background PDFs for the ee and $e\gamma$ samples. When a bracketed range is given, the parameter is allowed to float within that range. When a constant is given, the parameter is fixed to that constant.

PDF	Crystal Ball fit parameters				RooCMSShape fit parameters			
	μ	σ	α	n	μ	α	β	γ
ee signal	[86.2, 96.2]	[1.0, 5.0]	1.063	143.16	N/A	N/A	N/A	N/A
$e\gamma$ signal	[86.2, 96.2]	[1.0, 5.0]	1.063	143.16	N/A	N/A	N/A	N/A
ee background	N/A	N/A	N/A	N/A	58	97.0	0.0922	0.191
$e\gamma$ background	N/A	N/A	N/A	N/A	56	72.02	0.098	0.0375

Fits to the ee and $e\gamma$ invariant mass spectra are shown in Figure 1.20. Figure 1.21a indicates that there is some dependence of $f_{e\rightarrow\gamma}$ on the electron p_T, but since the the bulk of the electrons have $p_T \sim 45$ GeV, applying a p_T-dependent mis-identification rate has a negligible effect on the final background estimate. (Note that all fit parameters are floating in the p_T-dependent fits.) The dependence on η is small, as shown in Figure 1.21b. Therefore, a constant misidentification rate (derived from all ee and $e\gamma$ events), rather than a p_T- and η-dependent misidentification rate, is used in the final electroweak background estimate, with the difference between the constant rate and the rate for electrons with p_T between 25 and 40 GeV (the range in which the bulk of the trailing photons in the $\gamma\gamma$ sample lie) taken as a systematic error.

Using the integrals of the Z fits shown in Fig. 1.20, Eq. 1.7, and the p_T systematic

(a) *ee*.

(b) *eγ*.
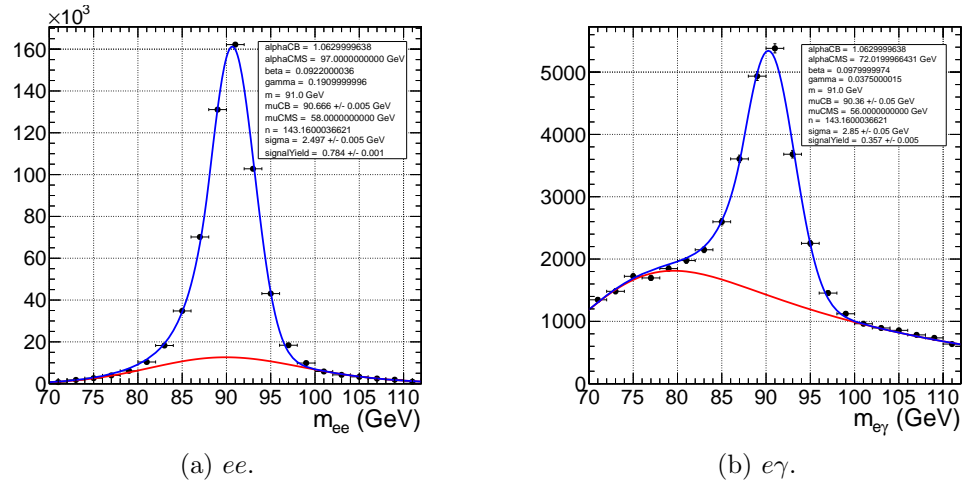
Figure 1.20: Fits to the *ee* and *eγ* invariant mass spectra using the Crystal Ball `RooCMSShape` function described in the text and in Table 1.3. The total fit is shown in blue, while the background component is shown in red.
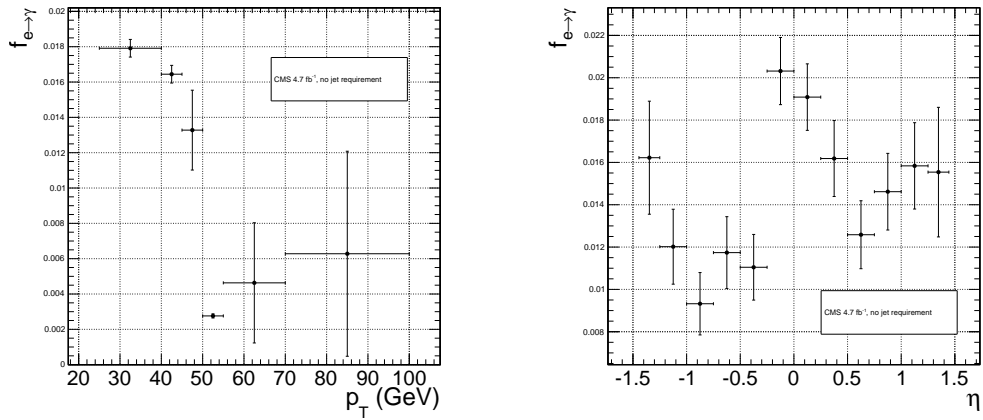
(a) $f_{e \to \gamma}$ vs. electron p_T. For the lowest p_T bin, the fit to the *eγ* spectrum does not converge well, so the Z signal fraction is fixed to the value in Fig. 1.20b.

(b) $f_{e \to \gamma}$ vs. electron η.

Figure 1.21: $f_{e \to \gamma}$ vs. electron p_T and η.

Figure 1.22: $\not{E}_T$ spectrum of the $e\gamma$ sample after scaling by $f_{e\to\gamma}$. The total error on $f_{e\to\gamma}$ is propagated to the total error on the electroweak background estimate.

discussed above, $f_{e\to\gamma}$ is calculated to be $0.014 \pm 0.000(\text{stat.}) \pm 0.004(\text{syst.})$. The scaled $e\gamma$ MET distribution is shown in Figure 1.22.

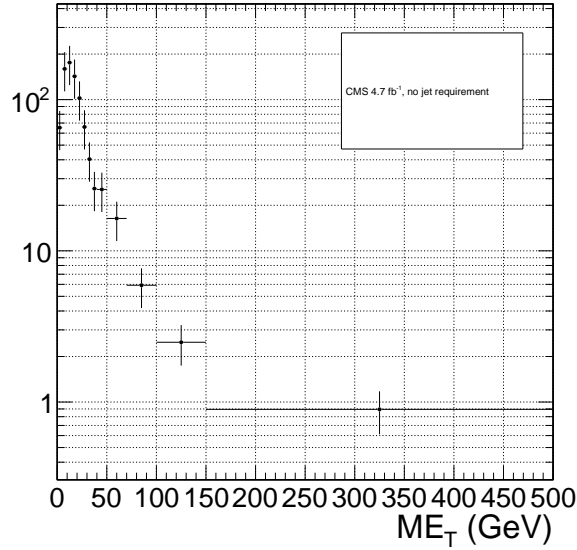In the 36 pb^{-1} version of this analysis [?], it was shown that the ee sample could accurately predict the QCD and real Z contribution to the $e\gamma$ sample at low $\not{E}_T$, and that the expectation from $W \to e\nu$ MC accounted for the remaining W contribution at high $\not{E}_T$. A plot of the $\not{E}_T$ distributions of the 2010 $e\gamma$ sample and the predicted components is shown in Figure 1.23. This exercise helps to validate both the QCD and electroweak background prediction methods.

1.4   Errors on the Background Prediction

The statistical error on the final background estimate in a particular $\not{E}_T$ bin comes from three sources: the number of control sample events collected in that bin, the statistical error on the weights applied to events in that bin, and the statistics of the normalization region. In the case of the ee control sample, there are contributions from the statistics of the m_{ee} sidebands as well.
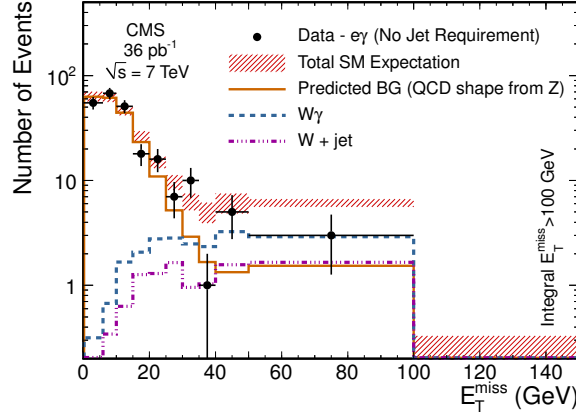
Figure 1.23: $\not{E}_T$ spectrum of the $e\gamma$ sample in 35 pb^{-1} of 2010 LHC data scaled by the 2010 measured $f_{e\to\gamma}$ (black dots), QCD and real Z predicted background from the 2010 ee sample (solid orange line), MC W + jet estimate (dash-dotted purple line), and MC $W\gamma$ estimate (dashed blue line). The total $e\gamma$ prediction (red band) is the sum of the ee, W + jet, and $W\gamma$ predictions. Reprinted from Fig. 2 of ref. [?].

In order to propagate the statistical error due to the reweighting procedure to the shape of the final QCD $\not{E}_T$ distribution, 1000 toy sets of weights are generated. Each set includes a weight for each (di-EM p_T, N_j) bin, with the values picked from a Gaussian distribution with mean and standard deviation equal to the observed weight for that bin and its statistical error. The effect of reweighting error is not correlated between $\not{E}_T$ bins. For each of the 1000 experiments, the control sample data are reweighted according to the generated weights, and the background estimates are calculated for each $\not{E}_T$ bin. Since the distribution of the toy background estimates follows a Gaussian distribution in each $\not{E}_T$ bin, the RMS spread of the estimates is taken as the statistical error due to reweighting. This procedure is carried out for the ff, ee, low sideband ee, and high sideband ee samples.

The total statistical error on the background estimate per $\not{E}_T$ bin is given by

$$\sigma_{\text{stat}}^2 = \sigma_{\text{stat,QCD}}^2 + \sigma_{\text{stat,EW}}^2 \qquad (1.8)$$

where $\sigma^2_{\text{stat,QCD}}$ is the square of the total statistical error on the QCD prediction in the $\not{E}_T$ bin

$$\sigma^2_{\text{stat,QCD}} = \sigma^2_{\text{stat},s} + \sigma^2_{\text{Poisson,QCD}} + \sigma^2_{\text{reweight},s} + \sigma^2_{\text{reweight,QCD}} \tag{1.9}$$

and $\sigma_{\text{stat,EW}}$ is the Poisson error on the number of $e\gamma$ events in the $\not{E}_T$ bin $(= \sqrt{N_{e\gamma}}$, where $N_{e\gamma}$ is the prediction in the $\not{E}_T$ bin after scaling by $f_{e\to\gamma}$). The contributions to $\sigma^2_{\text{stat,QCD}}$ are discussed below.

- $\sigma^2_{\text{stat},s}$ is the statistical error contributed by the normalization factor s (i.e. from Poisson error in the normalization region $\not{E}_T < 20$ GeV):

$$\begin{aligned}
\sigma^2_{\text{stat},s} &= \frac{N^2_{\text{control}}}{(N^{\text{norm}}_{\gamma\gamma} - N^{\text{norm}}_{e\gamma})^2}\left(\left[\sigma^{\text{norm}}_{\text{Poisson},\gamma\gamma}\right]^2 + \left[\sigma^{\text{norm}}_{\text{Poisson},e\gamma}\right]^2\right) + \\
&\quad \frac{N^2_{\text{control}}}{(N^{\text{norm}}_{\text{control}})^2}(\sigma^{\text{norm}}_{\text{Poisson,control}})^2
\end{aligned} \tag{1.10}$$

  where N_{control} is the number of reweighted, normalized events in the $\not{E}_T$ bin, $N^{\text{norm}}_{\gamma\gamma}$ is the number of $\gamma\gamma$ events in the normalization region, $N^{\text{norm}}_{e\gamma}$ is the number of $e\gamma$ events in the normalization region (after scaling by $f_{e\to\gamma}$), $\sigma^{\text{norm}}_{\text{Poisson},\gamma\gamma}$ is the Poisson error on the number of $\gamma\gamma$ events in the normalization region $(= \sqrt{N^{\text{norm}}_{\gamma\gamma}})$, $\sigma^{\text{norm}}_{\text{Poisson},e\gamma}$ is the Poisson error on the number of $e\gamma$ events in the normalization region $(= \sqrt{N^{\text{norm}}_{e\gamma}})$, $N^{\text{norm}}_{\text{control}}$ is the number of QCD control (ee or ff) events in the normalization region, and $\sigma^{\text{norm}}_{\text{Poisson,control}}$ is the Poisson error on the number of QCD control (ee or ff) events in the normalization region $(= \sqrt{\sum_{i=1}^{N^{\text{norm}}_{\text{control}}} w_i^2}$, where w_i is the di-EM p_T weight applied to event i). For the ee control region, N_{control} and $N_{\text{control,norm}}$ are sideband subtracted, and $\sigma^{\text{norm}}_{\text{Poisson,control}}$ includes the Poisson error on the number of sideband events.

- $\sigma_{\text{Poisson,QCD}}$ is the Poisson error due to the number of QCD control (*ee* or *ff*) events in the $\not{E}_T$ bin, equal to $\sqrt{\sum_{i=1}^{N_{\text{control}}} w_i^2}$, where w_i is the di-EM p_T weight applied to event i. For the *ee* control region, $\sigma_{\text{Poisson,QCD}}$ includes the Poisson error on the number of subtracted sideband events.

- $\sigma_{\text{reweight},s}$ is the error contributed by the control sample reweighting in the normalization region $(= \frac{N_{\text{control}}^2}{(N_{\text{control}}^{\text{norm}})^2} \sigma_{\text{reweight,control}}^{\text{norm}})$. $\sigma_{\text{reweight,control}}^{\text{norm}}$ is the quadrature sum of the RMS of the 1000 toy reweighting experiments for each $\not{E}_T$ bin in the normalization region. For the *ee* control sample, it also includes (in quadrature) the RMS of the toys in the sideband samples.

- $\sigma_{\text{reweight,QCD}}$ is the error contributed by the control sample reweighting in the $\not{E}_T$ bin $(= s\sigma_{\text{reweight,control}})$. $\sigma_{\text{reweight,control}}$ is the RMS of the 1000 toy reweighting experiments for the $\not{E}_T$ bin. For the *ee* control sample, it also includes (in quadrature) the RMS of the toys in the sideband samples.

The difference in hadronic activity between the *ee*, *ff*, and $\gamma\gamma$ samples results in a small bias ($\sim$1 GeV) of the *ee* $\not{E}_T$ distribution towards lower values with respect to the *ff* and $\gamma\gamma$ samples, as shown in Figure 1.24. Therefore, the *ff* sample is used as the primary QCD background estimator, and the difference between the *ee* and *ff* predictions is assigned as an error on the knowledge of the hadronic activity. For $\not{E}_T$ > 100 GeV, this error amounts to 43% of the total QCD + electroweak background estimate, and is the dominant source of systematic error.

The second largest source of systematic error comes from the p_T dependence of the $e \to \gamma$ misidentification rate (see 1.3). For $\not{E}_T$ > 100 GeV, the expected electroweak background is 3.4 $\pm$ 1.0 events, so this error amounts to 4.8% of the total QCD + electroweak background estimate.

The assumption of a constant $t\bar{t}$ and W + jets background shape under the Z peak in the *ee* sample induces a systematic error on the *ee* sideband-subtracted back-
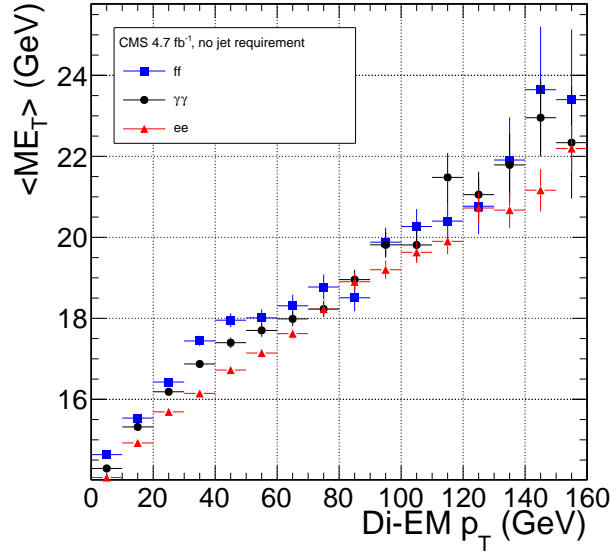
Figure 1.24: Average $\not{E}_T$ vs. di-EM p_T for the *ff* (blue squares), *ee* (red triangles), and $\gamma\gamma$ (black circles) samples.

ground prediction. To assess the magnitude of this error, the sideband subtraction (see Sec. 1.2.2) is performed once using only the prediction from the high sideband, and once using only the prediction from the low sideband. In each of these cases, the prediction is weighted by a factor of two, to account for the fact that the sideband regions are only half as wide (10 GeV) as the signal region (20 GeV). The maximum variation from the nominal *ee* estimate is taken as the error, which amounts to 11% for $\not{E}_T > 100$ GeV. $\not{E}_T$ distributions using the nominal *ee* sideband subtraction, the low-sideband-only subtraction, and the high-sideband-only subtraction are shown in Figure 1.25.

Finally, the few percent error on the jet energy correction factors introduces an error on the final background estimate through (a) the use of the PF p_T to measure the di-EM p_T, (b) the counting of jets passing a 30 GeV p_T threshold for placement of the event in an N_j bin for reweighting, and (c) the counting of jets above threshold for the $\geq$ 1-jet version of the selection. To estimate this error, 100 pseudo-experiments are generated with identical properties as the true data sample, except with corrected jet energies (in all events) all shifted by an amount $r\sigma(p_T, \eta)$. r is a random number
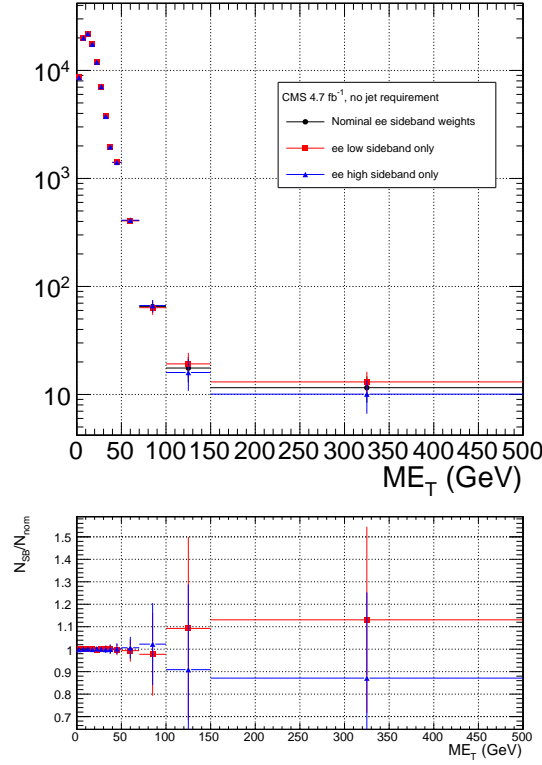
Added
this
para-
graph

Figure 1.25: *ee* $\not{E}_T$ distributions using the nominal sideband subtraction (black circles), low sideband only (red squares), and high sideband only (blue triangles). The bottom plot shows the ratio of the low sideband distribution to the nominal (red squares) and the ratio of the high sideband distribution to the nominal (blue triangles).

drawn from a Gaussian distribution with mean 0 and width 1, and $\sigma(p_T, \eta)$ is the uncertainty on the jet energy correction factor (which, like the correction factor itself, is a function of p_T and η). The same factor r is applied to all jets in all events in the pseudo-experiment because the jet energy correction errors are correlated from jet to jet (they result from e.g. uncertainties in MC simulation or uncertainties in ECAL energy scale [?]). The standard error of the mean of the 100 resulting background estimates in each relevant $\not{E}_T$ bin is taken as the error. The error in each $\not{E}_T$ bin is assumed to be uncorrelated. This process is repeated for both the inclusive and ≥ 1-jet selections. For $\not{E}_T \geq 100$ GeV, the jet energy correction uncertainty is 1.5%(2.2%) of the total background for the inclusive($\geq$1-jet) selection.

The uncertainty in how to define the (di-EM p_T, N_j) bins, especially at high di-
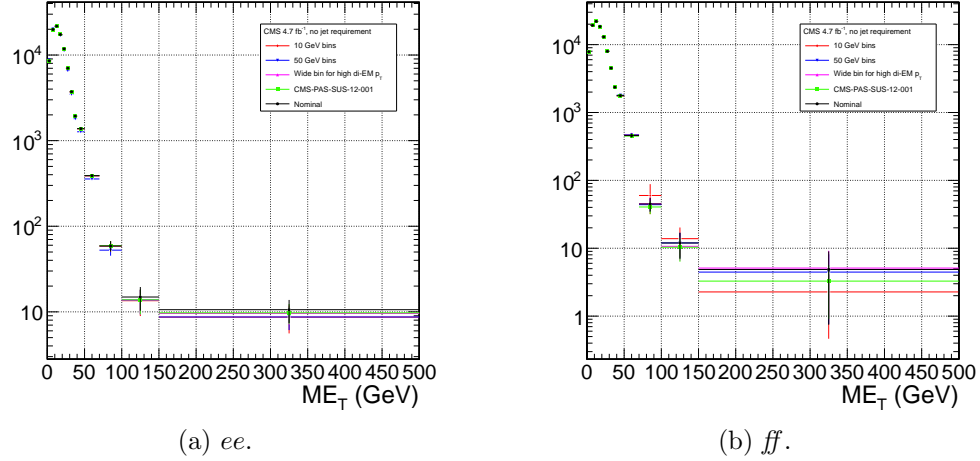
(a) *ee*. (b) *ff*.

Figure 1.26: Comparison of $\not{E}_T$ distributions for five different di-EM p_T bin definitions: uniform bins of width 10 GeV (red diamonds); uniform bins of width 50 GeV (blue downward-pointing triangles); bins with lower edges {0.0, 5.0, 10.0, 15.0, 20.0, 30.0, 40.0, 50.0, 60.0, 70.0, 80.0, 100.0, 750.0} GeV for 0-jet events and {0.0, 5.0, 10.0, 15.0, 20.0, 30.0, 40.0, 50.0, 60.0, 70.0, 80.0, 100.0, 120.0, 150.0, 200.0, 700.0} GeV for ≥1-jet events (magenta upward-pointing triangles), i.e. a single wide bin at high di-EM p_T; bins with lower edges {0.0, 5.0, 10.0, 15.0, 20.0, 30.0, 40.0, 50.0, 60.0, 70.0, 80.0, 100.0, 150.0} GeV for 0-jet events and {0.0, 5.0, 10.0, 15.0, 20.0, 30.0, 40.0, 50.0, 60.0, 70.0, 80.0, 100.0, 120.0, 150.0, 200.0} GeV for ≥1-jet events (green squares), i.e. the bins used in ref. [**?**]; and the nominal bin definitions shown in Fig. 1.19 (black circles).

EM p_T where the statistics are low, is covered by the 1000-toys procedure as long as the bins are not too coarse. This is shown in Figure 1.26. If the bins are too coarse, the details of the shape of the di-EM p_T spectra are lost, and the reweighting has a smaller effect.

The use of uncorrected instead of corrected PF $\not{E}_T$ (see Sec. **??**) makes no difference in the agreement of the background predictions and the search sample in a control region at low $\not{E}_T$, as shown in Figure 1.27. Since the control samples are derived from the same data as the search sample, any biases in the $\not{E}_T$ reconstruction due to jet energy scale are present equally in both samples.

Tables 1.4 and 1.5 list all the errors on the *ee* and *ff* QCD background predictions, respectively, for the $\not{E}_T$ bins used in the search. Table 1.6 lists the errors on the
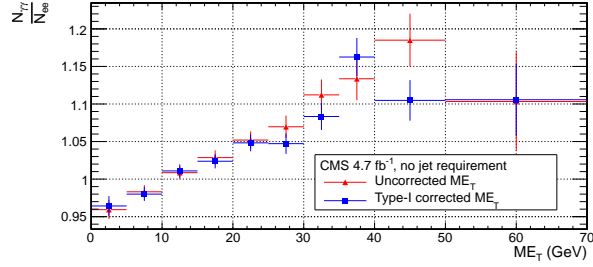
(a) Ratio of $\gamma\gamma$ to ee $\not{E}_T$ distributions.
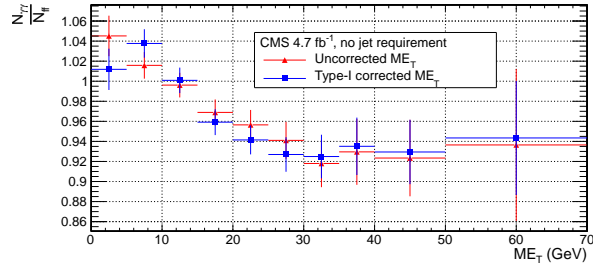
(b) Ratio of $\gamma\gamma$ to ff $\not{E}_T$ distributions.
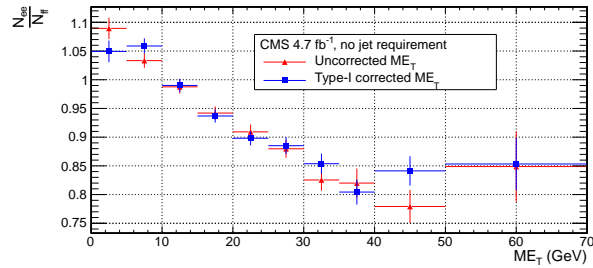
(c) Ratio of ee to ff $\not{E}_T$ distributions.

Figure 1.27: Agreement between $\gamma\gamma$, ee, and ff samples for uncorrected (red triangles) and corrected (blue squares) $\not{E}_T$.

electroweak background prediction. Finally, Table 1.7 shows the errors on the total QCD + electroweak background prediction, broken down by origin (statistical or systematic) and QCD background estimation sample (*ee* or *ff*). In the final result, only the *ff* QCD estimate is used.

Table 1.4: Errors on the *ee* QCD background prediction as a fraction of the *ee* prediction.

Source of error	Fractional uncertainty (%)				
	[50, 60)	[60, 70)	[70, 80)	[80, 100)	$\geq$100
Total	3.9	8.1	16	25	25
Statistics	3.6	7.8	16	24	22
No. events	3.6	7.7	15	24	20
In norm. region	0.43	0.44	0.46	0.55	0.51
In this $\not{E}_T$ bin	3.5	7.7	15	24	20
Reweighting	0.73	1.2	3.5	4.3	7.7
In norm. region	0.19	0.19	0.2	0.24	0.23
In this $\not{E}_T$ bin	0.71	1.2	3.5	4.3	7.7
Systematics	2.6	4.4	1.2	7.5	14
$f_{e \to \gamma}$ (in norm. region)	0.0012	0.0012	0.0013	0.0015	0.0014
m_{ee} background shape	1.4	2	0.72	5.5	12
Jet energy scale	2.2	3.9	0.96	5.1	6.9

1.5 Results

Figure 1.28(1.29) shows the $\not{E}_T$ distribution of the inclusive($\geq$1-jet) $\gamma\gamma$ search sample along with the predicted $\not{E}_T$ distributions of the QCD and electroweak backgrounds. The observed number of two-photon events, *ee* and *ff* background estimates and their errors, and expected number of inclusive($\geq$1-jet) two-photon events from two representative GGM SUSY models are listed in Table 1.8(1.9). (Details of the SUSY MC production are given in Chapter **??**.) The *ee* estimate is shown for comparison; the *ff* estimate is the official result used in the interpretation. No deviation from the Standard Model prediction is observed in the $\gamma\gamma$ search sample.

Table 1.5: Errors on the *ff* QCD background prediction as a fraction of the *ff* prediction.

Source of error	Fractional uncertainty (%)				
	[50, 60)	[60, 70)	[70, 80)	[80, 100)	$\geq$100
Total	15	25	61	34	64
Statistics	7.2	14	30	33	38
No. events	7.1	14	29	33	36
In norm. region	0.64	0.64	0.64	0.64	0.64
In this $\not{E}_T$ bin	7.1	14	29	33	36
Reweighting	0.85	2.7	5.1	6.9	13
In norm. region	0.27	0.27	0.27	0.27	0.27
In this $\not{E}_T$ bin	0.81	2.6	5.1	6.9	13
Systematics	13	21	53	6.6	52
ee/ff difference	13	21	53	5.5	52
$f_{e\to\gamma}$ (in norm. region)	0.0012	0.0012	0.0012	0.0012	0.0012
Jet energy scale	0.099	1.7	1.8	3.5	1.8

Table 1.6: Errors on the $e\gamma$ electroweak background prediction as a fraction of the $e\gamma$ prediction.

| Source of error	Fractional uncertainty (%)				
	[50, 60)	[60, 70)	[70, 80)	[80, 100)	$\geq$100
Total	29	29	30	30	30
Statistics	3.6	5.2	6.7	7.2	6.5
Systematics ($f_{e\to\gamma}$)	29	29	29	29	29

Table 1.7: Errors on the total QCD + electroweak background prediction as a fraction of the total prediction.

Source of error	Fractional uncertainty (%)				
	[50, 60)	[60, 70)	[70, 80)	[80, 100)	≥100
Total ($ee + e\gamma$)	3.9	7.8	15	22	22
Statistics	3.4	7.3	14	21	18
QCD	3.4	7.3	14	21	18
Electroweak	0.13	0.3	0.53	0.79	0.76
Systematics	2.7	4.5	2.6	7.4	13
QCD	2.5	4.1	1.1	6.7	12
Electroweak	1	1.7	2.3	3.2	3.4
Total ($ff + e\gamma$)	14	24	54	30	54
Statistics	6.9	13	26	29	30
QCD	6.9	13	26	29	30
Electroweak	0.11	0.24	0.79	0.83	1.1
Systematics	12	20	47	6.7	43
QCD	12	20	47	5.8	43
Electroweak	0.9	1.3	3.4	3.4	4.8

Table 1.8: Observed numbers of two-photon events, ee and ff background estimates and their errors, and expected numbers of two-photon events from two representative GGM SUSY models (details of MC simulation given in Chapter **??**) for the $\not{E}_T$ bins used in the search. The ee estimate is shown for comparison; the ff estimate is the official result used in the interpretation. Errors on the background estimates are detailed in Tables 1.4, 1.5, 1.6, and 1.7. Errors on the expected numbers of GGM events are purely statistical.
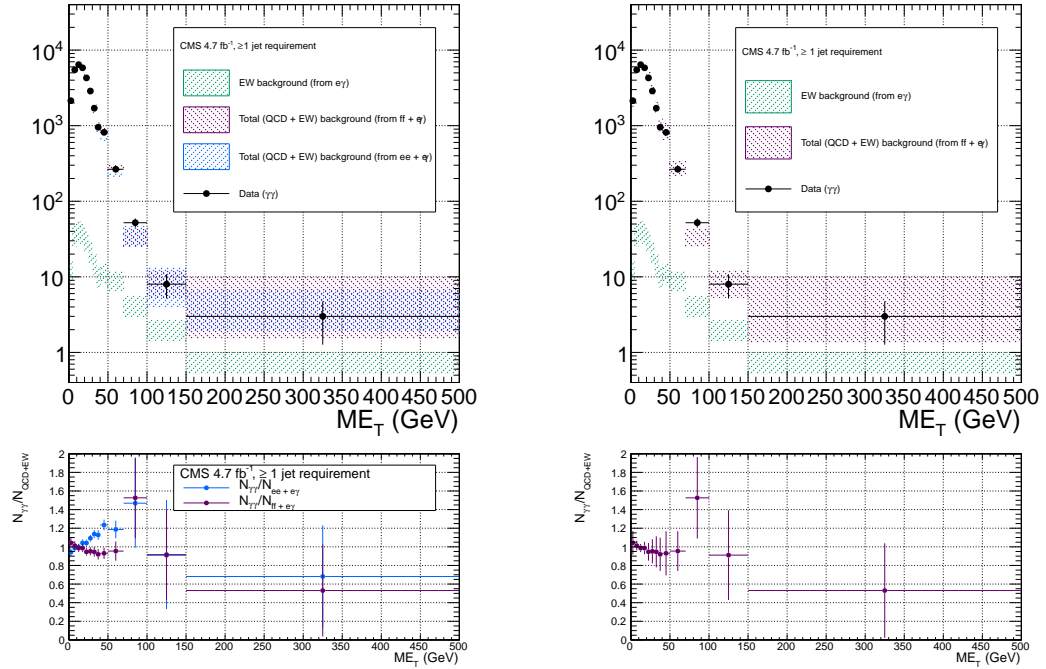
Source	No. events				
	[50, 60)	[60, 70)	[70, 80)	[80, 100)	≥100
Observation ($\gamma\gamma$)	354	93	37	33	17
Predicted background ($ff + e\gamma$)	361 ± 51.5	113 ± 27.1	26.9 ± 14.5	23.9 ± 7.23	20.2 ± 10.9
Predicted background ($ee + e\gamma$)	317 ± 14.1	90.2 ± 7.77	39.6 ± 5.75	25.1 ± 5.66	28.9 ± 6.70
$m_{\tilde{q}} = 720$ GeV $M_3 = 720$ GeV $M_1 = 375$ GeV	13.3 ± 2.13	17.7 ± 2.46	15.3 ± 2.33	42.9 ± 3.82	966 ± 18.3
$m_{\tilde{q}} = 1440$ GeV $M_3 = 1440$ GeV $M_1 = 375$ GeV	0.008 ± 0.003	0.009 ± 0.003	0.012 ± 0.003	0.030 ± 0.005	1.92 ± 0.04
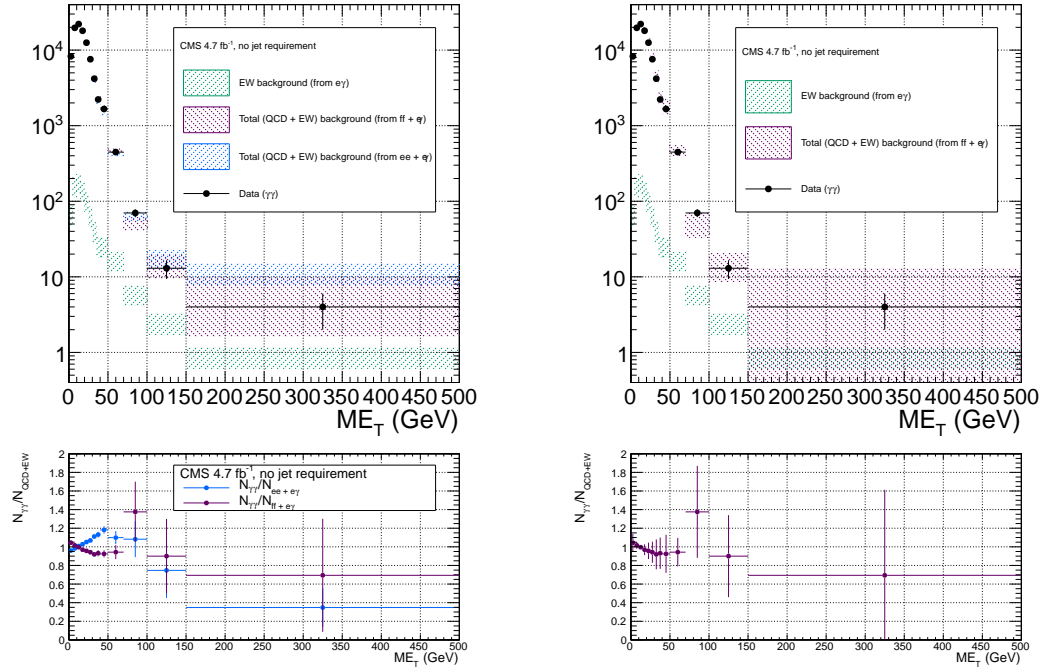
(a) $ee + e\gamma$ and $ff + e\gamma$. The widths of the bands correspond to the errors given in Table 1.7, excluding the error associated with the difference between the ee and ff QCD estimates for the $ff + e\gamma$ $\not{E}_T$ distribution.

(b) $ff + e\gamma$. The widths of the bands correspond to the errors given in Table 1.7, including the error associated with the difference between the ee and ff QCD estimates.

Figure 1.28: $\not{E}_T$ distribution of the $\gamma\gamma$ search sample (black circles) along with the predicted $\not{E}_T$ distributions of the QCD and electroweak backgrounds (blue band for ee QCD prediction + electroweak prediction, purple band for ff QCD prediction + electroweak prediction). The electroweak background prediction is shown in green. The bottom plots show the ratio of the $\gamma\gamma$ $\not{E}_T$ distribution to the $ee + e\gamma$ background distribution (blue) and $ff + e\gamma$ background distribution (purple).

(a) $ee + e\gamma$ and $ff + e\gamma$. The widths of the bands correspond to the errors given in Table 1.7, excluding the error associated with the difference between the ee and ff QCD estimates for the $ff + e\gamma$ $\not{E}_T$ distribution.

(b) $ff + e\gamma$. The widths of the bands correspond to the errors given in Table 1.7, including the error associated with the difference between the ee and ff QCD estimates.

Figure 1.29: $\not{E}_T$ distribution of the $\gamma\gamma + \geq 1$ jet search sample (black circles) along with the predicted $\not{E}_T$ distributions of the QCD and electroweak backgrounds (blue band for ee QCD prediction + electroweak prediction, purple band for ff QCD prediction + electroweak prediction). The electroweak background prediction is shown in green. The bottom plots show the ratio of the $\gamma\gamma$ $\not{E}_T$ distribution to the $ee + e\gamma$ background distribution (blue) and $ff + e\gamma$ background distribution (purple).

Table 1.9: Observed numbers of two-photon + ≥1-jet events, *ee* and *ff* background estimates and their errors, and expected numbers of two-photon + ≥1-jet events from two representative GGM SUSY models (details of MC simulation given in Chapter **??**) for the $\not{E}_T$ bins used in the search. The *ee* estimate is shown for comparison; the *ff* estimate is the official result used in the interpretation. Errors on the background estimates are detailed in Tables 1.4, 1.5, 1.6, and 1.7. Errors on the expected numbers of GGM events are purely statistical.

Source	No. events				
	[50, 60)	[60, 70)	[70, 80)	[80, 100)	≥100
Observation ($\gamma\gamma$ + ≥1 jet)	202	63	27	25	11
Predicted background (*ff* + $e\gamma$)	200 ± 35.4	77.7 ± 28.1	19.4 ± 8.55	14.7 ± 7.04	14.4 ± 5.59
Predicted background (*ee* + $e\gamma$)	171 ± 10.2	52.7 ± 5.74	25.1 ± 4.76	10.2 ± 5.04	13.1 ± 5.74
$m_{\tilde{q}} = 720$ GeV $M_3 = 720$ GeV $M_1 = 375$ GeV	13.3 ± 2.13	17.7 ± 2.46	15.3 ± 2.33	42.9 ± 3.82	965 ± 18.3
$m_{\tilde{q}} = 1440$ GeV $M_3 = 1440$ GeV $M_1 = 375$ GeV	0.008 ± 0.003	0.009 ± 0.003	0.012 ± 0.003	0.031 ± 0.004	1.92 ± 0.04